Nano Research
2019, 12(6): 1307–1312

ISSN 1998-0124 CN 11-5974/O4
https://doi.org/10.1007/s12274-018-2242-2

Research Article

Two-dimensional metal-organic-framework as a unique theranostic nano-platform for nuclear imaging and chemo-photodynamic cancer therapy

Wenjun Zhu[1,§], Yu Yang[2,§], Qiutong Jin[1], Yu Chao[1], Longlong Tian[1], Jingjing Liu[1], Ziliang Dong[1], and Zhuang Liu[1] (✉)

[1] *Institute of Functional Nano & Soft Materials (FUNSOM), Collaborative Innovation Center of Suzhou Nano Science and Technology, Jiangsu Key Laboratory for Carbon-based Functional Materials and Devices, Soochow University, Suzhou 215123, China*

[2] *State Key Laboratory of Quality Research in Chinese Medicine, Institute of Chinese Medical Sciences, University of Macau, Avenida da Universidad, Taipa, Macau 31608, China*

[§] *Wenjun Zhu and Yu Yang contributed equally to this work.*

Received: 11 September 2018 / **Revised:** 30 October 2018 / **Accepted:** 6 November 2018

ABSTRACT

Nanoscale metal organic frameworks (NMOFs) with porous structure and inherent biodegradability are attractive nanomedicine platforms. In addition to conventional particulate NMOFs, two-dimensional (2D) NMOFs are emerging as a unique type of NMOFs which however have been relatively less explored for nanomedicine applications. Herein, 2D NMOFs composed of Zn^{2+} and tetrakis(4-carboxyphenyl) porphyrin (TCPP) are fabricated and functionalized with polyethylene glycol (PEG). Compared to their particulate counterpart, such 2D NMOFs show greatly increased drug loading capacity and enhanced light-triggered singlet oxygen production, promising for chemotherapy and photodynamic therapy (PDT), respectively. Utilizing the porphyrin structure of TCPP, our 2D NMOFs could be labeled with a diagnostic radioisotope, ^{99m}Tc, for single photon emission computer tomography (SPECT) imaging, which reveals efficient tumor homing of those 2D NMOFs upon intravenous injection. While offering a remarkable synergistic *in vivo* antitumor effect for the combined chemo-PDT, such 2D NMOFs show efficient biodegradation and rapid renal clearance. Our work presents the great promise of 2D NMOFs for nanomedicine applications.

KEYWORDS

nanoscale metal-organic-framework, two-dimensional nanosheets, drug delivery, photodynamic therapy, combination therapy

1 Introduction

Nanoscale metal organic frameworks (NMOFs) and nanoscale coordination polymers (NCPs) are both hybrids of metal ions and organic ligands differing simply in their lattice structures. Over the past decade, NMOFs and NCPs have been widely explored by various fields owing to their tunable compositions, porous structures, and highly diverse functionalities [1–3]. In the area of nanomedicine, unlike conventional inorganic nanostructures, many of which are not biodegradable, NMOFs and NCPs show inherent biodegradability owing to the labile metal-organic coordination bonds [4, 5]. As multifunctional delivery systems or carrier-free nanoplatforms, NMOFs and NCPs could be employed for carrying chemotherapeutics [2, 6–8], gene therapeutics [9, 10], photothermal agents [11–13], photosensitizers [14–17] and imaging agents [18–20]. Thus, NMOFs and NCPs have emerged as a promising type of nanomaterials with great potential in nanomedicine and cancer theranostics [21, 22].

Typical two-dimensional (2D) nanomaterials including graphene and its derivatives [22–25], transitional metal disulfides [26], as well as MXenes [27], have received tremendous attention over the past decade owing to their ultra-thin structure and unique 2D morphology. In the area of nanomedicine, 2D nanomaterials with very high surface area and unique physicochemical properties have also been extensively explored for drug delivery and various cancer theranostic applications [28, 29]. Nanoscale 2D MOFs are a new member of the 2D materials family [30]. In a recent work, Zhang and co-workers reported the use of ultrathin 2D NMOF nanosheets as a fantastic fluorescence sensing platform for highly sensitive DNA detection [31]. However, the *in vivo* biomedical applications of 2D NMOF nanosheets have been relatively less explored to date. Whether such 2D nanostructures would exhibit any unique advantages in cancer theranostics over conventional particulate NMOFs or NCPs, remains to be further explored.

Herein, 2D NMOF nanosheets based on zinc cations (Zn^{2+}) and tetrakis(4-carboxyphenyl) porphyrin (TCPP) as the organic linker are synthesized, surface modified with polyethylene glycol (PEG), and exploited as a drug delivery carrier for *in vivo* combined chemo-photodynamic therapy. Compared to their counterpart, Zn-TCPP@PEG nanoparticles with exactly the same composition but particulate shape, 2D Zn-TCPP@PEG nanosheets exhibit obviously higher light-triggered singlet oxygen generation efficiency for enhanced photodynamic therapy (PDT), as well as significantly higher drug loading capacity for a chemotherapy drug, doxorubicin (DOX). Such phenomena are attributed to the unique 2D structure of those Zn-TCPP@PEG nanosheets with much larger surface area and easier accessibility to surrounding oxygen molecules. Utilizing the metal ion chelating ability of the porphyrin structure within TCPP, such Zn-TCPP@PEG nanosheets could be easily labeled with ^{99m}Tc, a gamma emission radioisotope, upon simple mixing, to enable quantitative *in vivo* tracking. As revealed by single photon emission computer tomography

Address correspondence to zliu@suda.edu.cn

(SPECT) imaging, those ^{99m}Tc-labeled Zn-TCPP@PEG/DOX nanosheets show efficient tumor retention upon intravenous (i.v.) injection. Thereafter, *in vivo* combined chemo-PDT treatment is conducted with i.v. injected Zn-TCPP@PEG/DOX, achieving a great synergistic anti-tumor efficacy. Importantly, such 2D NMOFs with inherent biodegradability exert no appreciable *in vivo* long-term toxicity. Therefore, our work highlights the great potential of 2D NMOFs as a biodegradable multifunctional nanoplatform with unique advantages in cancer theranostic applications.

2 Experimental

2.1 Materials

Zinc nitrate hexahydrate ($Zn(NO_3)_2{\cdot}6H_2O$) was purchased from MACKLIN. Pyrazine was purchased from Sigma-Aldrich. Polyvinylpyrrolidone K-30 (PVP) and tetrakis(4-carboxyphenyl) porphyrin (TCPP) were purchased from TCL, Shanghai, China. Doxorubicin (DOX) was purchased from Dalian Meilun Biotech Co., Ltd., China. PEG polymers were purchased from Jiaxin Bomei, Inc., China.

2.2 Fabrication of Zn-TCPP nanosheets and nanoparticles

To synthesis 2D Zn-TCPP nanosheets, 8.9 mg (0.03 mmol) $Zn(NO_3)_2{\cdot}6H_2O$, 0.8 mg (0.01 mmol) pyrazine and 20 mg PVP were dissolved in 12 mL mixture of DMF and ethanol (v/v = 3:1) in a 20 mL glass vial. After dissolution, 4 mg (0.005 mmol) TCPP in 4 mL mixture of DMF and ethanol (v/v = 3:1) was added dropwisely to the vial. Then, the mixture was ultrasonicated for 10 min and kept at 80 °C for 4 h. The light purple solid product was collected by 14,800 rpm centrifugation, washed by ethanol for three times and re-suspended in ethanol. Zn-TCPP nanoparticles were prepared following the same method but without the addition of PVP into the reaction system.

2.3 Drug loading and surface modification

Different amounts of DOX (0.05, 0.1 and 0.2 mg) in aqueous solutions were added to Zn-TCPP nanosheets or nanoparticles in 1 mL of ethanol solution ([TCPP]: 0.05 mg/mL). The mixture was kept at pH 8.0 by tris(hydroxymethyl) aminomethane—hydrochloric acid (Tris–HCl) buffer solution and stirred for 24 h. The products were washed by ethanol for five times to remove un-loaded DOX and dissolved in ethanol for future use. C18PMH-PEG polymer was synthesized following our previous protocol [32]. For surface modification, 1 mL Zn-TCPP nanosheets (or nanoparticles) without or with pre-loading of DOX in ethanol and 20 mg C18PMH-PEG in 1 mL ethanol were mixed together and stirred overnight at room temperature. The product was washed with distilled (DI) water for 3 times and was finally dissolved in 1 mL DI water.

2.4 Characterization

TEM images of Zn-TCPP@PEG nanosheets and nanoparticles were obtained by a FEI Tecnai F20 transmission electron microscope. The UV–visible–NIR spectrum were measured by a GENESYS 10S UV–Vis spectrophotometer. The hydrodynamic diameters of Zn-TCPP@PEG nanosheets and nanoparticles were measured byNano-ZS (Malvern Instruments, UK). The lattice of the two materials were determined by an X-ray diffractometer (PANalytical B.V.). The concentration of zinc cation (Zn^{2+}) was measured via inductively coupled plasma optical emission spectroscopy (ICP-OES, Thermo).

2.5 Measurement of singlet oxygen generation

To determine SO generation, 5 μL singlet oxygen sensor green (SOSG) was added to 1 mL aqueous solution of Zn-TCPP@PEG nanoparticles or nanosheets (50 μg/mL). The solutions were transferred into a 96-well plates and then exposed to a 660 nm light-emitting diode (LED) at 12 mW/cm^2 for different periods of time. Then the plates were measured to record the fluorescence intensities of SOSG in different samples.

2.6 Cellular experiment

Murine breast cancer 4T1 cells, murine colon cancer CT26 cells and human breast cancer MCF7 cells were all cultured under standard conditions recommended by the American Type Culture Collection (ATCC). The relative cell viabilities were measured by the standard methyl thiazolyl tetrazolium (MTT) assay. Confocal fluorescence images of cells were captured by using a Leica SP5 laser scanning confocal fluorescence microscope.

2.7 *In vitro* photodynamic therapy and combination therapy

4T1 cells seeded in 96-well plates (1×10^4 cells per well) were added with different concentrations of 2D Zn-TCPP@PEG or Zn-TCPP@PEG/DOX. After incubation for 24 h, the plates were exposed to a 660 nm LED (12 mW/cm^2) for 30 min (no light exposure as the control group). The MTT assay was carried out following the standard protocol.

2.8 Tumor model

All animal studies were conducted under the protocols approved by the Soochow University Laboratory Animal Center. The 4T1 subcutaneous tumors were planted by subcutaneous injection of 1×10^6 4T1 cells in ~ 50 μL PBS onto the back of each female Balb/c mouse. The mice were used when their tumor volumes reached about ~ 80 mm^3.

2.9 Blood circulation and biodistribution

Mice with 4T1 tumors were intravenous (i.v.) injected with Zn-TCPP@PEG/DOX ([TCPP]: 2.4 mg/mL, [Zn^{2+}]: 2.05 mg/mL, [DOX]: 0.5 mg/mL, 200 μL). Blood samples were taken at different periods of time. The mice were sacrificed at 24 h post-injection to collect main organs and tumors. All collected tissue samples were weighed and dissolved in digesting solutions (HNO_3:HCl:$HClO_4$ = 3:1:2 v/v) by heating for 2 h. The solutions were then diluted to 10 mL with DI water and measured via ICP-OES to determine the concentrations of Zn^{2+}. The background of Zn^{2+} in normal mice were subtracted during the calculation

$$\%ID/g = [Zn]_{tissue\ lysate} \times V_{tissue\ lysate}/(([Zn]_{injected} - [Zn]_{blank}) \times V_{injected} \times \text{tissue weight}) \times 100\%$$

2.10 Radiolabeling and *in vivo* SPECT imaging

2 mCi technetium-99m in the form of $^{99m}TcO_4$-(purchased from Shanghai GMS Pharmaceutical Co., Ltd) was added into 200 μL NMOF PBS solution ([TCPP]: 2.4 mg/mL, [DOX]: 0.5 mg/mL), in the presence of SnCl2 (10 mg/mL, 100 μL) to reduce $^{99m}TcO_4$– into $^{99m}Tc^{4+}$. Free ^{99m}Tc was removed by ultrafiltration. Mice with 4T1 tumors were i.v. injected with ^{99m}Tc labeled 2D NMOFs and imaged by *in vivo* animal SPECT imaging system (MILabs, Utrecht, the Netherlands) at different time points.

2.11 *In vivo* cancer therapy

Mice with 4T1 tumors were i.v. injected with different groups of 2D NMOFs ([TCPP]: 2.4 mg/mL, [DOX]: 0.5 mg/mL, 200 μL). After 24 h, tumors of mice were exposed to the 660 nm LED light (12 mW/cm^2) for an hour. The second treatment was repeated 5 days later. The tumor sizes were measured by a caliper every two days: volume = length × width^2/2. Relative tumor volume was calculated by V/V_0 (V_0 was the tumor volume when the treatment was initiated). For histological examination, the tumor tissues in each group were dissected two days after the first treatment to make paraffin sections

for hema-toxylin and eosin (H&E) staining. The major organs of mice receiving the combination therapy with Zn-TCPP@PEG/DOX were also dissected at day 12 for further H&E staining, with major organs collected from healthy mice used as controls.

2.12 Degradation

Mice i.v. injected with 2D NMOFs ([TCPP]: 2.4 mg/mL, [DOX]: 0.5 mg/mL, 200 μL) were treated with metabolic cages individually. Urine and feces were collected 0.5, 1, 2, 3 to 7 days. At the 7th day, mice were sacrificed for their major organs. Meanwhile, two different groups i.v. injected NMOFs were sacrificed at 1st and 3rd for their major organs. Urine, feces and organs of untreated mice were conducted to reduce the Zn^{2+} background. All samples were weighed and treated with digesting solutions for 2 h heating. The solutions were diluted to 10 mL for ICP analysis.

3 Result and discussion

In our work, both the nanoparticles and nanosheets were synthesized through the solvethermal method. In a typical method, 0.03 mmol zinc nitrate hexahydrate and 0.005 mmol TCPP were mixed with different amounts of poly(vinylpyrrolidone) (PVP, 30 kDa) in an 80 °C oven (Fig. 1(a)). As shown under transmission electron microscope (TEM), without adding PVP, particle-like Zn-TCPP MOFs were formed. Interestingly, by varying the amounts of PVP from 0 to 50 mg, the structure of those Zn-TCPP MOFs would be gradually altered from particle-like structure into the 2D nanosheet structure (Fig. 1(b)). With the addition of PVP to 50 mg, the TEM images showed relatively thin films in different orientaions (Fig. S1 in the Electronic Supplementary Material (ESM)). The atomic force microscopy (AFM) image also showed that such nanosheets had a thickness at about 2 nm (Fig. S2 in the ESM). Therefore, in order to get 2D NMOF nanosheets, PVP, which can selectively attach on the specific facets of the Zn-TCPP MOF, has to be added to block the MOF growth in one dimension [33], leading to the anisotropic growth of 2D Zn-TCPP NMOFs. Thereafter, we used an amphiphilic polymer, PEGylated poly(maleic anhydridealt-1-octadecene) (C_{18}PMH-PEG), to functionalize the obtained Zn-TCPP nanoparticles or nanosheets, to improve their stabilities in physiological solutions.

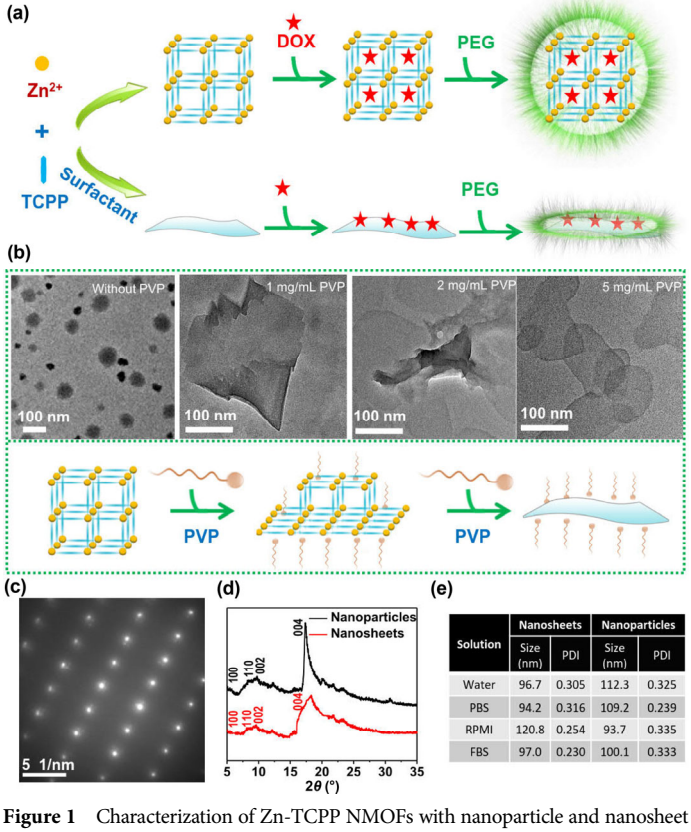

(e)

Solution	Nanosheets		Nanoparticles	
	Size (nm)	PDI	Size (nm)	PDI
Water	96.7	0.305	112.3	0.325
PBS	94.2	0.316	109.2	0.239
RPMI	120.8	0.254	93.7	0.335
FBS	97.0	0.230	100.1	0.333

Figure 1 Characterization of Zn-TCPP NMOFs with nanoparticle and nanosheet structures. (a) The synthesis procedure of Zn-TCPP NMOFs with the nanoparticle or nanosheet structure, as well as the subsequent PEG coating. (b) TEM images of Zn-TCPP with addition of different amounts of PVP. Below is the scheme to show the formation of 2D Zn-TCPP nanosheets. (c) SAED patterns of Zn-TCPP nanosheets. (d) XRD patterns of Zn-TCPP nanoparticles (black) and nanosheets (red). (e) Hydrodynamic diameters and polydispersity index (PDI) of Zn-TCPP@PEG nanosheets and nanoparicles in water, PBS, RPMI-1640 cell culture medium, and FBS 24 h after incubation measured by dynamic light scattering.

Careful characterizations were then conducted for the obtained NMOF products. The selected-area electron diffraction (SAED) pattern of 2D Zn-TCPP nanosheets was determined to be almost the same as that of Zn-TCPP nanoparticles [31], indicating the same crystal structure for the two types of NMOFs (Fig. 1(c)). In the powder X-Ray diffraction (XRD) spectrum, the characteristic peak at ~ 18° for the 2D Zn-TCPP sample was obviously broadened compared to that for its particulate counterpart (Fig. 1(d)), a phenomenon similar to that observed for other types of 2D nanosheets (e.g., MoS_2 and VS_2 nanosheets [34, 35]).

Next, the UV–Vis–NIR absorption spectra of free TCPP, Zn-TCPP@PEG nanoparticles and nanosheets were measured (Fig. S3 in the ESM). Compared to free TCPP, the Soret band absorption of Zn-TCPP@PEG nanoparticles and nanosheets showed obvious red-shifts. Notably, both Zn-TCPP@PEG nanosheets and nanoparticles showed high stability in physiological solutions including phosphate buffered saline (PBS), RPMI-1640 cell culture medium, and the fetal bovine serum (FBS), as revealed by the light scattering measurement of their hydrodynamic sizes (Fig. 1(e)).

Although 2D Zn-TCPP@PEG nanosheets had the same chemical composition of its particulate counterpart, we speculated that the two types of NMOFs may show distinctive PDT performances (Fig. 2(a)). The light-triggered reactive oxygen species (ROS)-singlet oxygen (SO) efficiencies of Zn-TCPP@PEG nanosheets and nanoparticles were estimated (Fig. 2(b)). Compared to Zn-TCPP@PEG nanoparticles, Zn-TCPP@PEG nanosheets exhibited obviously enhanced SO generation under 660-nm light irradiation (power density = 12 mW/cm^2). It is known that the enhancement of electron conduction and the reduction of self-quenching would be favorable for light-triggered SO generation in certain porphyrin-containing NMOFs [36]. Moreover, the unique 2D of Zn-TCPP@PEG could allow more efficient interactions of TCPP with surrounding oxygen molecules, resulting in stronger photodynamic effect for such 2D NMOFs compared to its particulate counterpart.

Next, *in vitro* cellular experiments were carried out to determine the PDT efficacy of our NMOFs. Without light exposure, both Zn-TCPP@PEG nanoparticles and nanosheets showed no appreciable dark toxicity to different types of cells (Fig. S4 in the ESM), suggesting the good biocompatibility of those NMOFs. As revealed by confocal images, both nanosheets and nanoparticles showed compared cellular uptake profiles (Fig. S5 in the ESM). The *in vitro* PDT efficacies of Zn-TCPP@PEG nanoparticles and nanosheets under light irradiation were then compared on 4T1 murine breast cancer cells (Fig. 2(c)). Interestingly, 2D Zn-TCPP@PEG nanosheets showed obviously increased light-triggered toxicity to cancer cells compared to that of Zn-TCPP@PEG nanoparticles at the same TCPP concentration. We then used confocal fluorescence microscope to evaluate the generation of reactive oxygen species (ROS) inside 4T1 cells by staining with the ROS-specific probe, 2,7-dichlorofluorescin diacetate (DCFH-DA) (Fig. 2(d)). Compared to cells incubated with Zn-TCPP@PEG nanoparticles after light irradiation, those incubated with Zn-TCPP@PEG nanosheets post light exposure showed remarkably increased intracellular ROS signals, which was also revealed by FACS assays from Fig. S6 in the ESM—The Zn-TCPP@PEG nanoparticles

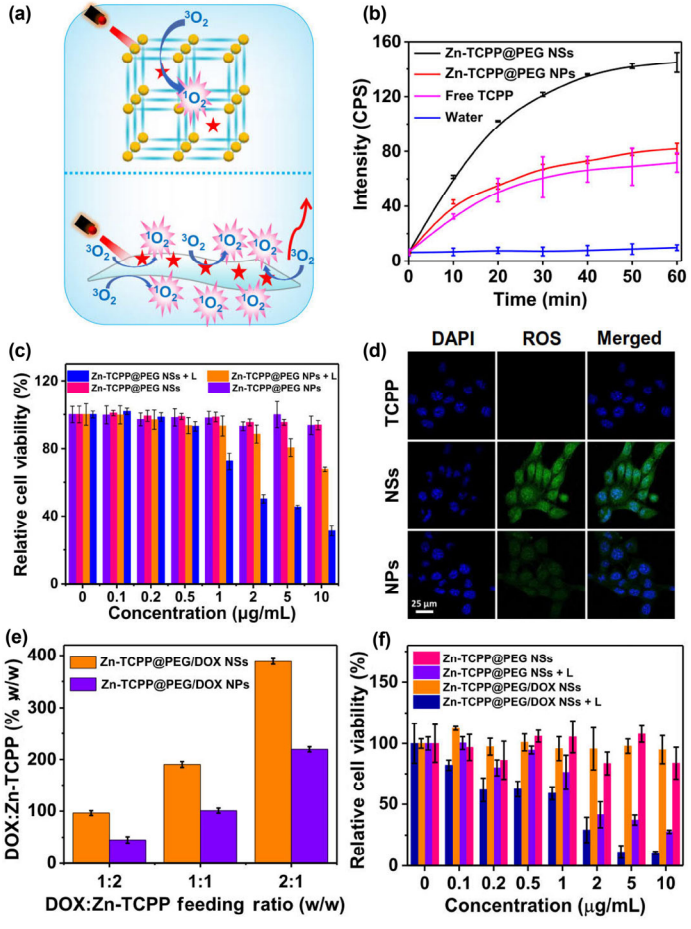

Figure 2 Comparison of Zn-TCPP@-PEG nanoparticles (NPs) and nanosheets (NSs) for PDT and drug delivery. (a) A scheme to compare the singlet oxygen generation and drug loading between Zn-TCPP@-PEG NPs and NSs. (b) SOSG fluorescence intensity of 2D Zn-TCPP@PEG NSs (black), Zn-TCPP@PEG NPs (red), free TCPP (pink) and water (blue) under light irradiation ([TCPP]: 50 μg/mL). (c) Relative viabilities of 4T1 cells treated with different concentrations of Zn-TCPP@PEG NPs or NSs under exposure to 660-nm light. (d) Confocal images to show light-triggered ROS generation inside cells incubated with Zn-TCPP@PEG NPs or NSs ([TCPP]: 1 μg/mL). (e) The drug loading mass percentage in different DOX feeding of 3D Zn-TCPP nanoparticles (purple) and 2D nanosheets (orange). (f) Relative viabilities of 4T1 cells treated with different concentrations (in terms of TCPP) of 2D Zn-TCPP@PEG or Zn-TCPP@PEG/DOX with or without 660-nm light exposure for 30 min at 12 mW/cm^2.

(NPs) had almost no DCFH-DA fluorescence while the nanosheets (NSs) group exhibited a much higher intensity. Therefore, the superior PDT efficacy of 2D Zn-TCPP@PEG nanosheets compared to their nanoparticle counterpart could be attributed to the stronger light-triggered SO generation ability of nanosheets.

NMOFs and NCPs with porous structures have been widely applied as drug delivery carriers. Therefore, we compared the drug loading capacities of Zn-TCPP@PEG nanosheets with nanoparticles side-by-side, using doxorubicin (DOX), a typical chemotherapy drug, as the model drug. As the increase of feeding mass ratios between NMOFs and DOX, the final drug loading ratios also showed gradual increase (Fig. 2(e)). Notably, the DOX loading capacities on Zn-TCPP@PEG nanosheets were found to be almost doubled compared to that on Zn-TCPP@PEG nanoparticles nanoparticles, likely owing to the much larger surface area of 2D NMOFs compared to that of particulate NMOFs.

With much more efficient light-triggered SO generation and higher DOX loading capacity, drug-loaded 2D NMOFs were then applied for *in vitro* combined chemo-PDT treatment. As revealed by the cell viability assay (Fig. 2(f)), 4T1 cells treated with 2D Zn-TCPP@PEG/DOX plus light irradiation (660 nm, 12 mW/cm^2, 30 min) showed the lowest viabilities in comparison to cells treated with Zn-TCPP@PEG/DOX in dark, as well as Zn-TCPP@PEG plus the same light exposure, under the same TCPP concentrations, demonstrating the high efficacy of combined chemo-PDT to kill cancer cells.

As porphyrin could form stable chelating complexes with many metal ions, we speculated that Zn-TCPP@PEG/DOX nanosheets might be labeled with radioisotope ions by forming chelates with the porphyrin ring within TCPP (Fig. 3(a)). ^{99m}Tc, a commonly used diagnostic radioisotope, was introduced in this study. As revealed from Fig. S7 in the ESM, the labelling stability remained about 75% 24 h post labelling. SPECT imaging was employed to track the *in vivo* translocation of ^{99m}Tc-labeled Zn-TCPP@PEG/DOX after i.v. injection into mice bearing 4T1 tumors (Fig. 3(b)). Based on the region-of-interest (ROI) value from SPECT images (Fig. 3(b), and different views from Fig. S8 in the ESM), apart from accumulation of such 2D NMOFs in the liver of mice, time-dependent tumor homing of NMOFs was also observed, a result from the enhanced permeability and retention (EPR) effect. The high signals in the heart indicated prolonged blood half-life of those 2D NMOFs. The tumor uptake of ^{99m}Tc-labeled 2D NMOFs was calculated to be ~ 7 %ID/g by statistically analyzing SPECT imaging data at 24 h post injection (Fig. 3(c)). In addition to SPECT imaging, *ex-vivo* fluorescent imaging for mice i.v. injected with Zn-TCPP@PEG/DOX (Fig. S9 in the ESM) also indicated the tumor accumulation of NMOFs *in vivo*. To further verify the imaging results, we quantitatively studied the

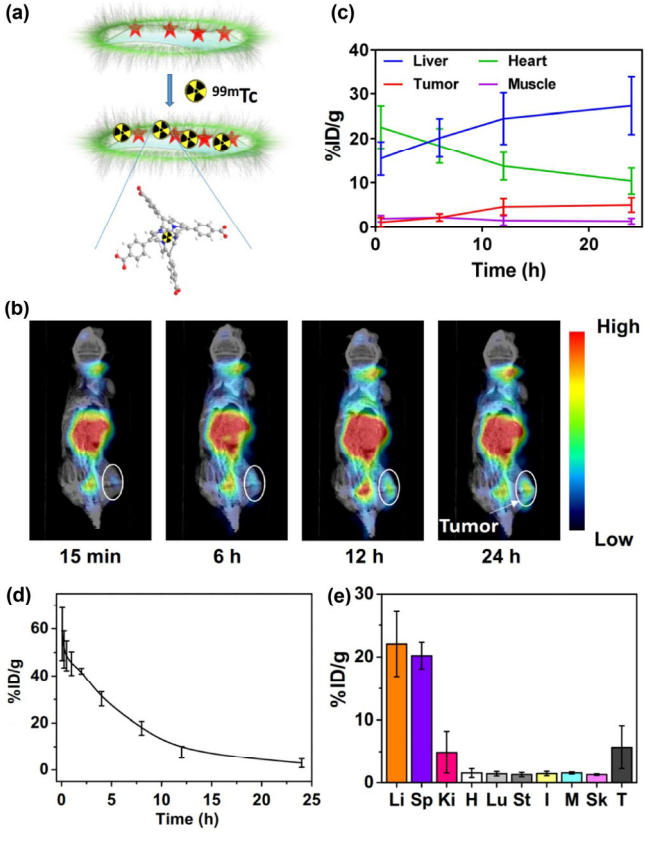

Figure 3 *In vivo* behaviors of 2D Zn-TCPP@PEG/DOX NMOFs. (a) A scheme to show ^{99m}Tc labeling of Zn-TCPP@PEG. (b) *In vivo* SPECT images of 4T1 tumor-bearing Balb/c mice post i.v. injection of ^{99m}Tc-Zn-TCPP@PEG/DOX 2D NMOFs. (c) Quantification of SPECT signals of ^{99m}Tc-Zn-TCPP@PEG/DOX in liver, heart, muscle and tumor of mice based on SPECT imaging data shown in (b). (d) Blood circulation profile of Zn-TCPP@PEG/DOX in mice after i.v. injection, as determined by ICP-measured Zn^{2+} concentrations in blood samples. (e) *Ex vivo* biodistribution profile of Zn-TCPP@PEG/DOX in mice determined by ICP-measured Zn^{2+} concentrations in various organs including liver (Li), spleen (Sp), kidney (Ki), heart (H), lung (Lu), stomach (St), intestine (I), muscle (M), skin (Sk) and tumor (T). Error bars are based on triplicated samples.

in vivo behaviors of such 2D NMOFs by measuring Zn^{2+} concentrations in blood and tissue samples via ICP-OES. Such Zn-TCPP@PEG/DOX nanosheets showed relatively long blood circulation half-lives ($t_{1/2}\alpha$ = 3.66 ± 0.27 h, $t_{1/2}\beta$ = 3.81 ± 0.26 h) (Fig. 3(d)), consistent to the SPECT imaging data regarding high signals in the heart. The tumor uptake of Zn-TCPP@PEG/DOX was determined to be ~ 5% ID/g (Fig. 3(e)), similar to that measured by SPECT imaging data.

The *in vivo* chemo-PDT combination therapy was then carried out for Balb/c mice bearing 4T1 tumor. Mice were divided into five groups (5 mice per group) randomly: 1) untreated control group, 2) i.v. injection with free DOX, 3) i.v. injection with Zn-TCPP@PEG/DOX nanosheets, 4) i.v. injection with Zn-TCPP@PEG nanosheets + light irradiation, 5) i.v. injection with Zn-TCPP@PEG/DOX nanosheets + light irradiation The doses of TCPP and DOX were fixed at 24 and 5 mg/kg, respectively. PDT was conducted by 660-nm light irradiation (12 mW/cm^2) at 24 h after i.v. injection, lasting for one hour. The second treatment was given 5 days after the first injection following the same parameters. After receiving various treatments, the tumor volumes were carefully measured every two days (Fig. 4(a)), and the tumors of various treatment groups were collected and weighed at day 12 post treatment (Fig. 4(b)). Compared to untreated group and free DOX treated group, the mice treated by Zn-TCPP@PEG/DOX without 660-nm light irradiation showed partial inhibitory effect on the tumor growth. Meanwhile, PDT treatment with Zn-TCPP@PEG plus light also exhibited a moderate tumor growth inhibition effect. Interestingly, we found that mice treated with Zn-TCPP@PEG/DOX plus light showed excellent tumor growth inhibition effect, demonstrating the remarkable synergistic effect of the combined PDT and chemotherapy, which might result from the synergistic effect of PDT and chemotherapy in such dose. The irradiation of Zn-TCPP might contribute to the decomposition of nanosheets and thus contribute to the release of DOX. Moreover, PDT has been reported to enhanced EPR effect and thus enhance the accumulation of such nanosheets [37].

Next, H&E staining of tumor slices (Fig. 4(c)) further confirmed the most effective tumor cell destruction in the group with combined chemo-PDT delivered by Zn-TCPP@PEG/DOX. In addition, no obvious toxicity of the combination therapy was observed in the experiment group according to the H&E stained organ slices from the chemo-PDT combination therapy group collected at day 12 after the treatment with Zn-TCPP@PEG/DOX plus light (Fig. 4(d)). No appreciable body weight drop was also noticed for mice injected with Zn-TCPP@PEG/DOX (Fig. S10 in the ESM).

To further verify the excretion profiles of 2D NMOFs, long-time biodegradation experiments were conducted. The Zn^{2+} levels in different organs of mice post i.v. injection of Zn-TCPP@PEG were measured by ICP-OES (Fig. 4(e)). Although relatively high levels of Zn^{2+} in the mouse liver and spleen were noted at 1 day post injection, a rapid increase of Zn^{2+} concentrations in mouse organs was observed. After one week, the retention of Zn^{2+} in various mouse organs was found to become rather lower, suggesting efficient clearance of such NMOFs from the mouse body. Additionally, it was found that most of Zn^{2+} can be excreted, particularly by urine within the first 7 days post i.v. injection of Zn-TCPP@PEG (Fig. 4(f)). Therefore, our results collectively suggest that such 2D NMOFs after systemic administration into animals would be degraded into small molecules and ions, which are then rapidly excreted primarily via renal excretion without much long-term retention.

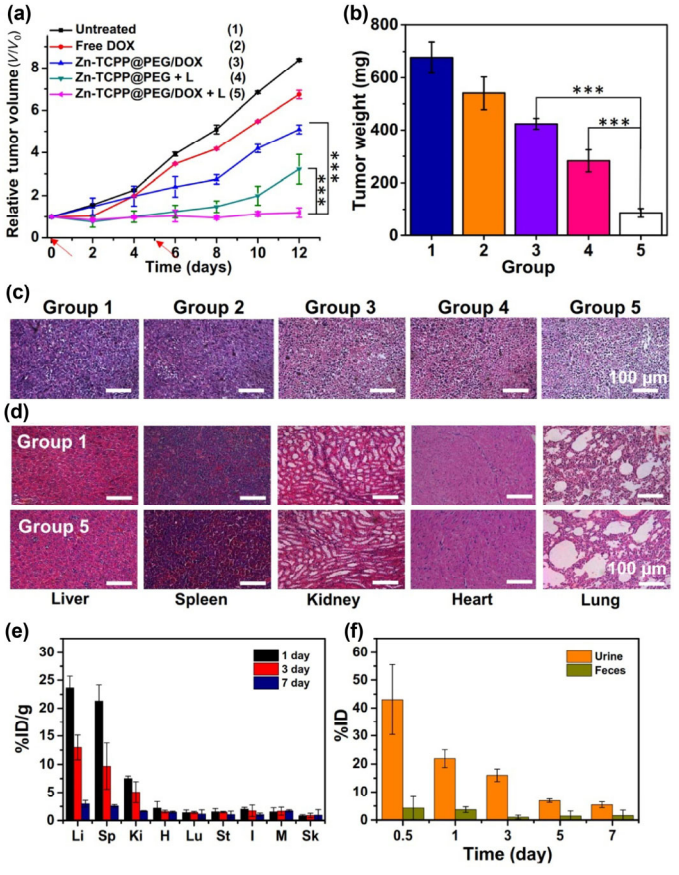

Figure 4 *In vivo* combination therapy with 2D Zn-TCPP@PEG/DOX NMOFs. (a) Tumor growth curves for different groups of mice: (1) control, (2) i.v. injection with free DOX, (3) i.v. injection with Zn-TCPP@PEG/DOX, (4) i.v. injection with Zn-TCPP@PEG + Light, (5) i.v. injection with Zn-TCPP@PEG/DOX + Light. (b) Average tumor weights collected at day 12 for different groups of mice. Error bars are based on standard deviations of five mice per group. *P* values were calculated by Tukey's post-test (***P < 0.001, **P < 0.01). (c) H&E stained images of tumor slices collected 2 days after receiving different treatments. (d) H&E stained images of major organs from mice at the 12th day for the control group (group 1) and the combination therapy group (group 5). (e) Biodistribution of Zn-TCPP@PEG/DOX measured 1, 3, and 7 days post i.v. injection by ICP-OES. The examined organs include liver (Li), spleen (Sp), kidney (Ki), heart (H), lung (Lu), stomach (St), intestine (I), muscle (M), skin (Sk). Error bars are based on triplicated samples. (f) Excretion profiles of Zn^{2+} from Zn-TCPP@PEG/DOX injected mice measured in urine and feces collected at different time post injection.

4 Conclusion

In this work, we have demonstrated that 2D NMOFs could be a unique type of nano-platform for cancer theranostic applications. Compared to particulate NMOFs, such 2D Zn-TCPP@PEG NMOF nanosheets are superior not only in higher drug loading capacity, but also in more efficient light-triggered SO production, representing enormous potential for chemotherapy and photodynamic therapy, respectively. Utilizing the porphyin structure of TCPP, the drug-loaded 2D NMOFs could be easily labeled with ^{99m}Tc to enable *in vivo* SPECT imaging, which illustrates the time-dependent tumor homing of Zn-TCPP@PEG/DOX nanosheets post i.v. injection. Rather effective *in vivo* anti-tumor therapeutic effect is achieved after the combined chemo-PDT treatment with such drug-loaded 2D NMOFs. Importantly, those NMOF nanosheets with inherent biodegradability show rapid excretion and exert little *in vivo* toxicity. In conclusion, such nanoplatfrom offers an efficient anti-tumor efficacy in mice by chemo-PDT therapy with low bio-toxicity, which might give the potential for clinical application by its multifunctional structure, low toxicity and rapid clearance. Our work therefore highlights the unique superiorities of 2D NMOFs as a new class of multifunctional biodegradable theranostic nano-platforms.

Acknowledgements

This work was partially supported by the National Research Programs from Ministry of Science and Technology (MOST) of China (No.

2016YFA0201200), the National Natural Science Foundation of China (Nos. 51525203 and 51761145041), Collaborative Innovation Center of Suzhou Nano Science and Technology, and a Project Funded by the Priority Academic Program Development (PAPD) of Jiangsu Higher Education Institutions.

Electronic Supplementary Material: Supplementary material (attached with all the supporting figures mentioned in this work) is available in the online version of this article at https://doi.org/10.1007/s12274-018-2242-2.

References

[1] He, C. B.; Liu, D. M.; Lin, W. B. Nanomedicine applications of hybrid nanomaterials built from metal-ligand coordination bonds: Nanoscale metal-organic frameworks and nanoscale coordination polymers. *Chem. Rev.* **2015**, *115*, 11079–11108.

[2] Della Rocca, J.; Liu, D. M.; Lin, W. B. Nanoscale metal–organic frameworks for biomedical imaging and drug delivery. *Acc. Chem. Res.* **2011**, *44*, 957–968.

[3] Li, H. L.; Eddaoudi, M.; O'Keeffe, M.; Yaghi, O. M. Design and synthesis of an exceptionally stable and highly porous metal-organic framework. *Nature* **1999**, *402*, 276–279.

[4] Furukawa, H.; Cordova, K. E.; O'Keeffe, M.; Yaghi, O. M. The chemistry and applications of metal-organic frameworks. *Science* **2013**, *341*, 1230444.

[5] Horcajada, P.; Chalati, T.; Serre, C.; Gillet, B.; Sebrie, C.; Baati, T.; Eubank, J. F.; Heurtaux, D.; Clayette, P.; Kreuz, C. et al. Porous metal-organic-framework nanoscale carriers as a potential platform for drug delivery and imaging. *Nat. Mater.* **2010**, *9*, 172–178.

[6] Huxford, R. C.; Della Rocca, J.; Lin, W. B. Metal–organic frameworks as potential drug carriers. *Curr. Opin. Chem. Biol.* **2010**, *14*, 262–268.

[7] Horcajada, P.; Serre, C.; Vallet-Regí, M.; Sebban, M.; Taulelle, F.; Férey, G. Metal–organic frameworks as efficient materials for drug delivery. *Angew. Chem.* **2006**, *118*, 6120–6124.

[8] McKinlay, A. C.; Morris, R. E.; Horcajada, P.; Férey, G.; Gref, R.; Couvreur, P.; Serre, C. Biomofs: Metal–organic frameworks for biological and medical applications. *Angew. Chem., Int. Ed.* **2010**, *49*, 6260–6266.

[9] Tafipolsky, M.; Schmid, R. Systematic first principles parameterization of force fields for metal–organic frameworks using a genetic algorithm approach. *J. Phys. Chem. B* **2009**, *113*, 1341–1352.

[10] Morris, W.; Briley, W. E.; Auyeung, E.; Cabezas, M. D.; Mirkin, C. A. Nucleic acid–metal organic framework (MOF) nanoparticle conjugates. *J. Am. Chem. Soc.* **2014**, *136*, 7261–7264.

[11] Yang, Y.; Zhu, W. J.; Dong, Z. L.; Chao, Y.; Xu, L.; Chen, M. W.; Liu, Z. 1D coordination polymer nanofibers for low–temperature photothermal therapy. *Adv. Mater.* **2017**, *29*, 1703588.

[12] Yang, Y.; Chao, Y.; Liu, J. J.; Dong, Z. L.; He, W. W.; Zhang, R.; Yang, K.; Chen, M. W.; Liu, Z. Core-shell and co-doped nanoscale metal-organic particles (NMOPs) obtained via post-synthesis cation exchange for multimodal imaging and synergistic thermo-radiotherapy. *NPG Asia Mater.* **2017**, *9*, e344.

[13] Yang, Y.; Liu, J. J.; Liang, C.; Feng, L. Z.; Fu, T. T.; Dong, Z. L.; Chao, Y.; Li, Y. G.; Lu, G.; Chen, M. W. et al. Nanoscale metal–organic particles with rapid clearance for magnetic resonance imaging-guided photothermal therapy. *ACS Nano* **2016**, *10*, 2774–2781.

[14] Liu, J. J.; Yang, Y.; Zhu, W. W.; Yi, X.; Dong, Z. L.; Xu, X. N.; Chen, M. W.; Yang, K.; Lu, G.; Jiang, L. X. et al. Nanoscale metal–organic frameworks for combined photodynamic & radiation therapy in cancer treatment. *Biomaterials* **2016**, *97*, 1–9.

[15] Lu, K. D.; He, C. B.; Lin, W. B. A chlorin-based nanoscale metal–organic framework for photodynamic therapy of colon cancers. *J. Am. Chem. Soc.* **2015**, *137*, 7600–7603.

[16] Park, J.; Jiang, Q.; Feng, D. W.; Mao, L. Q.; Zhou, H. C. Size-controlled synthesis of porphyrinic metal–organic framework and functionalization for targeted photodynamic therapy. *J. Am. Chem. Soc.* **2016**, *138*, 3518–3525.

[17] Yu, B.; Wei, H.; He, Q. J.; Ferreira, C. A.; Kutyreff, C. J.; Ni, D. L.; Rosenkrans, Z. T.; Cheng, L.; Yu, F. Q.; Engle, J. W. et al. Efficient uptake of ^{177}Lu–porphyrin–PEG nanocomplexes by tumor mitochondria for multimodal–imaging–guided combination therapy. *Angew. Chem., Int. Ed.* **2018**, *57*, 218–222.

[18] Lebedev, O. I.; Millange, F.; Serre, C.; Van Tendeloo, G.; Férey, G. First direct imaging of giant pores of the metal–organic framework MIL-101. *Chem. Mater.* **2005**, *17*, 6525–6527.

[19] Taylor, K. M. L.; Rieter, W. J.; Lin, W. B. Manganese-based nanoscale metal-organic frameworks for magnetic resonance imaging. *J. Am. Chem. Soc.* **2008**, *130*, 14358–14359.

[20] Taylor-Pashow, K. M. L.; Rocca, J. D.; Xie, Z. G.; Tran, S.; Lin, W. B. Postsynthetic modifications of iron-carboxylate nanoscale metal–organic frameworks for imaging and drug delivery. *J. Am. Chem. Soc.* **2009**, *131*, 14261–14263.

[21] He, C. B.; Lu, J. Q.; Lin, W. B. Hybrid nanoparticles for combination therapy of cancer. *J. Control. Release* **2015**, *219*, 224–236.

[22] Pastorin, G.; Wu, W.; Wieckowski, S.; Briand, J. P.; Kostarelos, K.; Prato, M.; Bianco, A. Double functionalisation of carbon nanotubes for multimodal drug delivery. *Chem. Commun.* **2006**, *11*, 1182–1184.

[23] Cao, A. N.; Liu, Z.; Chu, S. S.; Wu, M. H.; Ye, Z. M.; Cai, Z. W.; Chang, Y. L.; Wang, S. F.; Gong, Q. H.; Liu, Y. F. A facile one-step method to produce graphene–CdS quantum dot nanocomposites as promising optoelectronic materials. *Adv. Mater.* **2010**, *22*, 103–106.

[24] Yang, K.; Zhang, S.; Zhang, G. X.; Sun, X. M.; Lee, S. T.; Liu, Z. Graphene in mice: Ultrahigh *in vivo* tumor uptake and efficient photothermal therapy. *Nano Lett.* **2010**, *10*, 3318–3323.

[25] Yang, K.; Feng, L. Z.; Shi, X. Z.; Liu, Z. Nano-graphene in biomedicine: Theranostic applications. *Chem. Soc. Rev.* **2013**, *42*, 530–547.

[26] Lv, R. T.; Robinson, J. A.; Schaak, R. E.; Sun, D.; Sun, Y. F.; Mallouk, T. E.; Terrones, M. Transition metal dichalcogenides and beyond: Synthesis, properties, and applications of single-and few-layer nanosheets. *Acc. Chem. Res.* **2014**, *48*, 56–64.

[27] Naguib, M.; Mochalin, V. N.; Barsoum, M. W.; Gogotsi, Y. 25th anniversary article: Mxenes: A new family of two–dimensional materials. *Adv. Mater.* **2014**, *26*, 992–1005.

[28] Yin, W. Y.; Yan, L.; Yu, J.; Tian, G.; Zhou, L. J.; Zheng, X. P.; Zhang, X.; Yong, Y.; Li, J.; Gu, Z. J. et al. High-throughput synthesis of single-layer MoS_2 nanosheets as a near-infrared photothermal-triggered drug delivery for effective cancer therapy. *ACS Nano* **2014**, *8*, 6922–6933.

[29] Lai, H. Q.; Zhang, X.; Feng, P. J.; Xie, L. N.; Chen, J. J.; Chen, T. F. Enhancement of antiangiogenic efficacy of iron(II) complex by selenium substitution. *Chem. Asian J.* **2017**, *12*, 982–987.

[30] Peng, Y.; Li, Y. S.; Ban, Y. J.; Jin, H.; Jiao, W. M.; Liu, X. L.; Yang, W. S. Metal-organic framework nanosheets as building blocks for molecular sieving membranes. *Science* **2014**, *346*, 1356–1359.

[31] Zhao, M. T.; Wang, Y. X.; Ma, Q. L.; Huang, Y.; Zhang, X.; Ping, J. F.; Zhang, Z. C.; Lu, Q. P.; Yu, Y. F.; Xu, H. et al. Ultrathin 2D metal-organic framework nanosheets. *Adv. Mater.* **2015**, *27*, 7372–7378.

[32] Prencipe, G.; Tabakman, S. M.; Welsher, K.; Liu, Z.; Goodwin, A. P.; Zhang, L.; Henry, J.; Dai, H. J. PEG branched polymer for functionalization of nanomaterials with ultralong blood circulation. *J. Am. Chem. Soc.* **2009**, *131*, 4783–4787.

[33] Choi, E. Y.; Wray, C. A.; Hu, C. H.; Choe, W. Highly tunable metal–organic frameworks with open metal centers. *CrystEngComm* **2009**, *11*, 553–555.

[34] Wang, K. P.; Wang, J.; Fan, J. T.; Lotya, M.; O'Neill, A.; Fox, D.; Feng, Y. Y.; Zhang, X. Y.; Jiang, B. X.; Zhao, Q. Z. et al. Ultrafast saturable absorption of two-dimensional MoS_2 nanosheets. *ACS Nano* **2013**, *7*, 9260–9267.

[35] Feng, J.; Sun, X.; Wu, C. Z.; Peng, L. L.; Lin, C. C.; Hu, S. L.; Yang, J. H.; Xie, Y. Metallic few-layered VS_2 ultrathin nanosheets: High two-dimensional conductivity for in-plane supercapacitors. *J. Am. Chem. Soc.* **2011**, *133*, 17832–17838.

[36] Lu, K. D.; He, C. B.; Lin, W. B. Nanoscale metal-organic framework for highly effective photodynamic therapy of resistant head and neck cancer. *J. Am. Chem. Soc.* **2014**, *136*, 16712–16715.

[37] Fan, W. P.; Yung, B.; Huang, P.; Chen, X. Y. Nanotechnology for multimodal synergistic cancer therapy. *Chem. Rev.* **2017**, *117*, 13566–13638.